Stably stratified turbulence in the presence of large-scale forcing

C. Rorai, P. D. Mininni, and A. Pouquet

Phys. Rev. E **92**, 013003 — Published 6 July 2015

DOI: 10.1103/PhysRevE.92.013003

Stably stratified turbulence in the presence of large-scale forcing

C. Rorai[1], P.D. Mininni[2] and A. Pouquet[3,4]
[1] *Nordita, Roslagstullsbacken 23, 106 91 Stockholm, Sweden;*
[2] *Departamento de Física, Facultad de Ciencias Exactas y Naturales, Universidad de Buenos Aires & IFIBA, CONICET, Ciudad Universitaria, 1428 Buenos Aires, Argentina;*
[3] *National Center for Atmospheric Research, P.O. Box 3000, Boulder CO 80307 USA;*
[4] *Department of Applied Mathematics, University of Colorado, Boulder CO 80309-256 USA.*

We perform two high resolution direct numerical simulations of stratified turbulence for Reynolds number equal to $Re \approx 25000$ and Froude number respectively of $Fr \approx 0.1$ and $Fr \approx 0.03$. The flows are forced at large scale and discretized on an isotropic grid of 2048^3 points. Stratification makes the flow anisotropic and introduces two extra characteristic scales with respect to homogeneous isotropic turbulence: the buoyancy scale, L_B, and the Ozmidov scale, ℓ_{oz}. The former is related to the number of layers that the flow develops in the direction of gravity, the latter is regarded as the scale at which isotropy is recovered. The values of L_B and ℓ_{oz} depend on the Froude number, and their absolute and relative amplitudes affect the repartition of energy among Fourier modes in non easily predictable ways. By contrasting the behavior of the two simulated flows we identify some surprising similarities: after an initial transient the two flows evolve towards comparable values of the kinetic and potential enstrophy, and energy dissipation rate. This is the result of the Reynolds number being large enough in both flows for the Ozmidov scale to be resolved. When properly dimensionalized, the energy dissipation rate is compatible with atmospheric observations. Further similarities emerge at large scales: the same ratio between potential and total energy (≈ 0.1) is spontaneously selected by the flows, and slow modes grow monotonically in both regimes causing a slow increase of the total energy in time. The axisymmetric total energy spectrum shows a wide variety of spectral slopes as a function of the angle between the imposed stratification and the wave vector. One-dimensional energy spectra computed in the direction parallel to gravity are flat from the forcing up to buoyancy scale. At intermediate scales a $\sim k^{-3}$ parallel spectrum develops for the $Fr \approx 0.03$ run, whereas for weaker stratification, the saturation spectrum does not have enough scales to develop and instead one observes a power law compatible with Kolmogorov scaling. Finally, the spectrum of helicity is flat until L_B, as observed in the nocturnal planetary boundary layer.

I. INTRODUCTION

Geophysical fluid dynamics, as encountered in the atmosphere and the oceans, is at the center of our understanding and predicting capabilities in weather and climate. The modes that prevail in such systems are a mixture of nonlinear eddies and waves; specifically, inertial waves when a solid-body rotation is considered, and internal gravity waves when stratification is present. The nonlinear coupling between these modes leads to extreme events which are both sporadic and spatially localized, with steep gradients in the velocity and temperature or density fields, a phenomenon observed both in the stable planetary boundary layer [1], as well as in high-resolution direct numerical simulations (DNS) of the Bousinesq equations [2]. Nonlinear interactions are also associated with other phenomena, such as wave steepening and breaking, instabilities (as the Kelvin-Helmoltz instability), and turbulent cascades. As these interactions take place in a wide range of scales, and as timescales in geophysical flows are not homogeneous in scale, universality (as is the case in homogeneous isotropic turbulence) is not necessarily obtained in such complex flows. It is then of interest to identify features of such flows that are robust to changes in the parameters and characteristic timescales.

A. The case of stratified turbulence

In this study we focus our attention on stably stratified flows, for which two relevant timescales can be identified: the gravity wave period, $\tau_\omega \approx 1/N$, and the eddy turnover time, $\tau_{\rm NL} \approx L_F/u_{\rm rms}$; here N, $u_{\rm rms}$, and L_F are respectively the Brunt-Väisälä frequency, the r.m.s. velocity, and the characteristic lengthscale of the flow. Whether the flow is dominated by gravity waves or by eddies depends on the relative values of τ_ω and $\tau_{\rm NL}$. In practice, the fastest timescale is expected to dominate the dynamics. However, as already mentioned, these timescales are not homogeneous across length scales, and even if the waves dominate over the eddies at large scales, the two timescales may become comparable at a smaller scale. For stratification, the scale at which these two characteristic times are equal is called the Ozmidov scale $\ell_{\rm oz} = 2\pi/k_{\rm oz}$, with $k_{\rm oz} = (N^3/\varepsilon)^{1/2}$ and with ε the energy dissipation rate. Beyond $\ell_{\rm oz}$, isotropy and a classical Kolmogorov range is expected.

Another characteristic scale for stably stratified flows is the buoyancy scale, defined by $L_B = 2\pi/k_B$ with $k_B = N/u_{rms}$, and associated with the number of layers that the flow forms in the direction of gravity. The scale η, at which dissipation sets in (of the order of the centimeters or the millimeters in the atmosphere and the oceans), marks the end of the turbulence regime. The presence of two additional characteristic scales (ℓ_{oz} and L_B) with

respect to the case of homogeneous and isotropic turbulence suggests a much richer and complex picture, consisting of different and multiple dynamical regimes across scales. Are these regimes clearly identifiable and distinguishable? What are their characteristics in terms of energy spectra? Is the transition between them effectively marked by the scales defined above? These are the general questions that we aim to address, with a special focus on those quantities that remain unchanged in two configurations with different parameters.

In approaching this problem numerically we face numerous challenges. We chose to study the direct cascade inertial range, that is, the behavior of scales smaller than the forcing scale (a previous work focused on the inverse cascade in rotating and/or stratified flows [3]). Hence, we inject energy at large scale. To be able to distinguish the possible different regimes we need a large separation between the forcing, buoyancy, Ozmidov, and dissipation scales, which calls for computationally intensive, high Reynolds number calculations (with $Re = u_{rms}L_F/\nu$). The Froude number $Fr = u_{rms}/(L_F N)$ needs to be selected carefully; it has to be sufficiently small to guarantee enough scale separation between k_B and k_{oz} (in fact, $k_{oz}/k_B \propto 1/\sqrt{Fr}$), but at the same time it has to be large enough to allow the observation of the recovery of isotropy before dissipation sets in at scale k_η, considering that $k_\eta/k_{oz} \propto Fr^{3/2}Re^{3/4}$. We thus propose to study forced stratified turbulence using DNS at a resolution of 2048^3 points, and to contrast the evolution for two different stratification strengths, $Fr \approx 0.03$ and 0.1, by varying only the ratio of the wave period to the eddy turn-over time, namely $\tau_\omega/\tau_{\rm NL}$, by a factor 3.

B. Recent numerical studies

One can find many reviews concerning stratified turbulence (see, e.g., [4–8]). Some important concepts emerged from detailed numerical studies with different settings (e.g., comparing two-dimensional vs. three-dimensional forcing, with the forcing acting at large scale or at small scale, balanced or not, etc.); see [9–15]. Also, several large DNS considered the stratified case in the presence of shear [16, 17], or of rotation [18–20].

It is now known that in stratified turbulence in boxes with unit aspect ratio, the kinetic energy undergoes a direct cascade to small scales, and its spectrum follows at sufficiently small scales a Kolmogorov-like law in terms of $k_\perp$ (i.e., of wavevectors perpendicular to gravity) [21]. At small scales, the buoyancy field is believed to follow an equivalent law, similar to that of a passive scalar. The spectra in terms of $k_\parallel$ seem to follow a steeper $\sim k_\parallel^{-3}$ law, often called the saturation spectrum. Flat spectra at large scale, presumably larger than the buoyancy scale L_B, are also reported. However, different simulations with varying configurations and parameters present different behavior.

In [10] a large-scale two-dimensional forcing is used, with grids up to $1024^2 \times 320$ points. Computations are performed at high Reynolds number and small Froude number, varying the buoyancy Reynolds number $\mathcal{R}_B = ReFr^2$. Two regimes are identified, for low or high $\mathcal{R}_B$, with steep spectra and laminar layers in the former case, and the $k_\perp^{-5/3}$ spectra for kinetic and potential energy and turbulent layers in the latter case. These findings confirm previous works (see [10] for a detailed review), and are often put in the context of atmospheric observations. Similarly, oceanic measurements of eddy diffusivity have identified two regimes of mixing, in terms of the same parameter [22, 23]. Using larger grid resolution and hyper-viscosity but similar forcing, it is shown in [11] that resolving or not the buoyancy scale may affect the outcome as far as energy distribution among Fourier modes is concerned, with steeper spectra when L_B is well resolved, and that there is a sharp spectral break at the buoyancy scale as already predicted by [24]. Note that steep spectra mean that non-local interactions between widely separated modes are dominant. Moreover, when energy spectra are steeper than k^{-2}, dissipation takes place predominantly at large scale, and one cannot properly talk of an energy cascade phenomenon in the sense that dissipation acts over the entire spectrum.

In [12] the choice is made of a cubic grid of 1024^3 points, and the spectral data is also analyzed in terms of the wave-vortical decomposition introduced in [25, 26]. The spectra are found to be flat at large scale, a feature explained through the accumulation of sharp layers in the vertical direction. In [13] large DNS on grids of up to $4096^2 \times 2048$ points are performed, and in these runs the Ozmidov scale is resolved. The horizontal spectra appear to follow again a $k_\perp^{-5/3}$ law, and it is noted that the direct cascade in the vertical direction provides a pathway to dissipation and to the generation of layers in the flow. The results also indicate the layers are such that the Froude number based on the vertical scale is of order unity [27], a feature already observed empirically in [28]. These results are confirmed by yet higher resolution runs [14, 15] at unit Prandtl number and with buoyancy Reynolds numbers of up to 220. Such a high resolution allows also for a detailed investigation of intermittency. Finally, in [9], it is confirmed that the critical parameter to determine what scaling exponents prevail in the spectra is the buoyancy Reynolds number: at large Reynolds number, the spectra are found to be independent of stratification.

What can be concluded from these past studies is that a consensus has not yet been reached as to whether there will be a universal description of such flows. In the present paper, we show that, as suggested already in [29], some of the ambiguities found in preceding studies are linked to a competition between several phenomena, namely on one hand the growth of slow modes with $k_\perp \approx 0$, and on the other hand the dynamics of fast modes with $k_\perp \neq 0$.

II. METHODS

A. The Boussinesq equations

The dynamics of a turbulent flow in a stably stratified environment can be described by the incompressible Navier-Stokes equations under the Boussinesq approximation. According to this model the three-dimensional velocity field $\mathbf{u}(\mathbf{x},t)$ of Cartesian components (u,v,w), and the temperature fluctuations (or buoyancy field) $\theta(\mathbf{x},t)$ obey the set of equations

$$\partial_t \mathbf{u} + \mathbf{u}\cdot\nabla\mathbf{u} = -\nabla P - N\theta\ e_z + \nu\Delta\mathbf{u} + \mathbf{f}_V, \quad (1)$$

$$\partial_t \theta + \mathbf{u}\cdot\nabla\theta = Nw + \kappa\Delta\theta, \quad (2)$$

$$\nabla\cdot\mathbf{u} = 0; \quad (3)$$

where P is the pressure, N the Brunt-Väisälä frequency, ν the viscosity, $\mathbf{f}_V$ a velocity forcing term, and κ the thermal diffusivity. As customary, the Brunt-Väisälä frequency is defined by $N=\sqrt{-(g/\theta_0)(d\bar{\theta}/dz)}$, where g is the gravitational acceleration, θ_0 is the mean temperature, and $\bar{\theta}$ is a linear temperature profile.

Note that the temperature fluctuations are written in units of velocity through the change of variable $\theta = \theta' g/(N\theta_0)$, where θ' are the temperature fluctuations in units of temperature. We make the equations dimensionless by dividing velocity, space, and time by a characteristic velocity $\overline{U}$, a characteristic length $\overline{L}$, and the characteristic turnover time $\overline{\tau}=\overline{L}/\overline{U}$. We solve the equations in a cubic domain of length $L_0/\overline{L}=2\pi$. For the choice $\overline{L}=1$, the wavenumber in Fourier space associated with L_0 is unitary, and all the larger wavenumbers are integers. The Brunt-Väisälä frequency is $N=\overline{N}\,\overline{\tau}$. The viscosity, $\nu=\overline{\nu}/(\overline{L}\,\overline{U})$, should also be regarded as dimensionless, and similarly for the thermal diffusivity; note that with our choice of $\overline{U}$ and $\overline{L}$, the former can be interpreted as the inverse of a Reynolds number.

The Boussinesq approximation is often used to study stably stratified atmospheric and oceanic flows. For a detailed discussion on the validity and limitations of this approximation for the ocean see, e.g., [30] and references therein.

B. Global quantities

The system can be characterized in terms of its energy, helicity, enstrophy, and dissipation rate, expressed either as a function of time or of Fourier space wavenumbers. The mean total energy E_T is defined as the sum of the kinetic E_V and potential E_P energy

$$\frac{1}{2}\left\langle |\mathbf{u}|^2 + \theta^{\,2}\right\rangle = E_V + E_P = E_T,$$

and is a conserved quantity in the ideal limit. The brackets indicate the spatial mean. We also define helicity, the velocity-vorticity correlation, as

$$H_V = \langle \mathbf{u}\cdot\omega\rangle\,.$$

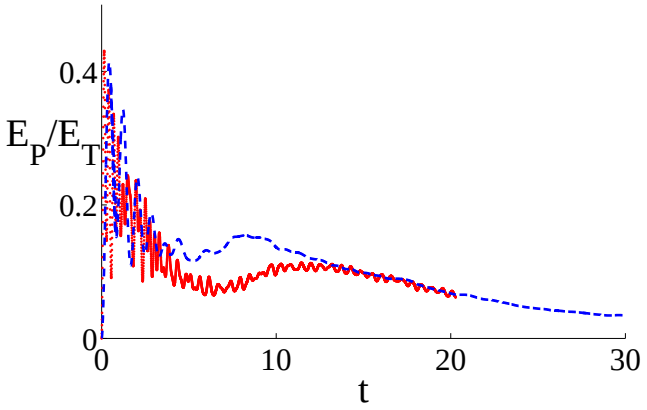

FIG. 1. *(Color online)* Temporal evolution of the ratio between potential and total energy for the runs with $Fr\approx 0.1$ ($N=4$, dashed, blue line) and $Fr\approx 0.03$ ($N=12$, solid, red line). The oscillatory phase lasts longer for the more strongly stratified flow, but both ratios take comparable values after a transient.

Helicity is an invariant of the inviscid non-stratified equations and has been observed to considerably slow-down the decay of turbulent energy in the presence of stratification [31], as well as with rotation [32, 33]; it can also be created under the combined effects of rotation and stratification [34, 35].

The kinetic enstrophy, proportional to the kinetic energy dissipation, is given by $Z_V=\langle\omega^2\rangle$. Similarly, the potential enstrophy is $Z_P=\langle|\nabla\theta|^2\rangle$ and is associated with the dissipation of potential energy. As only the velocity field is forced, the total injection rate is simply given by

$$\varepsilon_V = \langle \mathbf{u}\cdot\mathbf{f}_V\rangle\,. \quad (4)$$

In the turbulent steady state, this quantity is expected to be equal (on the time average) to the total dissipation rate $\nu\langle\omega^2\rangle+\kappa\langle|\nabla\theta|^2\rangle$.

C. Spectral quantities

We now define the reduced energy and helicity spectra. In Fourier space the velocity autocorrelation function is noted $U_{ij}(k_x,k_y,k_z)$ and its trace is $U(\mathbf{k})$. Hence the axisymmetric kinetic energy spectrum is

$$e_V(|\mathbf{k}|,\Theta) = \int U(\mathbf{k})|\mathbf{k}|\sin\Theta d\phi, \quad (5)$$

where ϕ is the longitude with respect to the k_x axis, and Θ is the co-latitude. By defining parallel $k_\parallel=k_z$, perpendicular $k_\perp=|\mathbf{k}_\perp|=|\mathbf{k}|\sin\Theta$, and isotropic $k=|\mathbf{k}|$ wavenumbers, we can calculate parallel, perpendicular, and isotropic reduced kinetic energy spectra respectively

as follows [36]

$$E_V(k_\parallel) = \int e_V(|\mathbf{k}_\perp|, k_\parallel) dk_\perp, \quad (6)$$

$$E_V(k_\perp) = \int e_V(|\mathbf{k}_\perp|, k_\parallel) dk_\parallel, \quad (7)$$

$$E_V(k) = \int e_V(|\mathbf{k}|, \Theta) |\mathbf{k}| d\Theta. \quad (8)$$

Similar definitions hold for the potential and total energy, and for the helicity spectrum $h(|\mathbf{k}|, \Theta)$, which is related to the antisymmetric part of the velocity correlation tensor [36].

We can also distinguish between slow and fast mode spectra, namely:

$$E_{V,\text{slow}} = e_V(|\mathbf{k}_\perp| = 0, k_\parallel), \quad (9)$$

$$E_{V,\text{fast}} = \int_{k_\parallel=0}^{k_{\parallel\max}} \int_{|k_\perp|=1}^{|k_\perp|_{\max}} e_V(|\mathbf{k}_\perp|, k_\parallel) dk_\perp dk_\parallel. \quad (10)$$

Equivalent definitions hold for $E_{P,\text{slow}}$, $E_{P,\text{fast}}$, $E_{T,\text{slow}}$, and $E_{T,\text{fast}}$. The slow modes satisfy the condition $\omega = 0$, where ω is the frequency of gravity waves given by the dispersion relation $\omega = \sqrt{N^2 k_\perp^2}/k$. These modes correspond to "pure" eddies (vortical motions), and their characteristic timescale is the eddy turnover time. When $Fr < 1$, the waves at large scales are faster than the eddies, or in other words, the wave period is faster than the turnover time. This is why the remaining modes, which correspond to a combination of eddies and waves, are often called "fast" modes.

Finally, the fluxes of kinetic and potential energy are respectively given by:

$$\Pi_V(k) = \int_0^k \Gamma(k') dk', \quad (11)$$

$$\Pi_P(k) = \int_0^k \mathrm{P}(k') dk', \quad (12)$$

with $\Gamma(k) = \mathbf{u}^\star(k) \cdot \mathcal{F}(\mathbf{u} \cdot \nabla \mathbf{u})_k$ and $\mathrm{P}(k) = \mathbf{u}^\star(k) \cdot \mathcal{F}(\theta \nabla \theta)_k$, where $\mathcal{F}$ denotes the Fourier transform. As explained in more detail below, the total flux $\Pi = \Pi_V + \Pi_P$ measures the amount of energy that goes through a given wavenumber per unit of time.

D. Initial conditions and forcing

Equations (1) to (3) are solved numerically in a cubic domain with an isotropic grid of 2048^3 points using the pseudo-spectral Geophysical High-Order Suite for Turbulence (GHOST) code, which is parallelized with hybrid MPI/OpenMP programming [37], and has now been tested on over 100,000 compute cores. The code is based on a 2^{nd}–order explicit Runge-Kutta temporal scheme, and uses a standard 2/3 de-aliasing rule in Fourier space.

The initial condition and the velocity forcing, $\mathbf{f}_V$, consist of randomly generated isotropic three-dimensional flows [38] with injection wave number k_F between 2 and 3. The forcing has amplitude $f_{\text{rms}} = 0.22$, chosen to yield an approximately unitary r.m.s. velocity ($u_{\text{rms}} = 1$) in the turbulent steady state. We impose $\nu = 10^{-4}$, which guarantees that the Kolmogorov scale for a homogeneous isotropic flow with the same parameters and discretization is well resolved [39]. Note this is a conservative choice, since in wave turbulence the energy spectrum is expected to be steeper, and therefore the small scales are expected to be less energetic. As a result of these choices, the ratio between the smallest and largest scales resolved in our calculations is about ≈ 700, and the Reynolds number is $Re \approx 25000$.

As mentioned in the introduction, we perform two runs with different values of the Brunt-Väisälä frequency, resulting in $Fr \approx 0.1$ (for $N = 4$), and $Fr \approx 0.03$ (for $N = 12$). The buoyancy Reynolds number $\mathcal{R}_B = ReFr^2$ is correspondingly $\mathcal{R}_B = 250$ and $\mathcal{R}_B = 27$. The calculations are carried out for respectively 30 and 20 time units. Finally, in both runs we consider a unitary Prandtl number $Pr = \nu/\kappa = 1$.

E. Characteristic scales

For our simulations of stratified flows, the relevant length scales are:

(i) The overall size of the periodic domain, equal to $L_0 = 2\pi$ in dimensionless units, and with associated wavenumber $k_0 = 2\pi/L_0$.

(ii) The scale at which energy is injected into the system, $L_F = 2\pi/k_F$.

(iii) The buoyancy scale, $L_B = 2\pi/k_B$, with $k_B = N/u_{\text{rms}}$, characteristic of the vertical shear.

(iv) The scale at which isotropy (and presumably a Kolmogorov energy spectrum) is recovered, namely the Ozmidov scale $\ell_{\text{oz}} = 2\pi/k_{\text{oz}}$, with $k_{\text{oz}} = (N^3/\varepsilon)^{1/2}$.

(v) The dissipation scale, $\eta = 2\pi/k_\eta$, with $k_\eta = (\varepsilon/\nu^3)^{1/4}$.

(vi) The smallest scale resolved in the DNS, namely $\ell_{\min} = 2\pi/k_{\max}$. Because of the Fourier transform the pseudospectral code is based upon, and the 2/3-rule for removing aliasing $k_{\max} = n/3 \approx 700$ where n is the number of grid points per dimension.

In Table I we report the values of the wavenumbers associated with these characteristic scales.

The Ozmidov and the dissipation scales are usually evaluated by estimating $\varepsilon \approx u_{\text{rms}}^3/L_F$. However, this estimation is valid for isotropic and homogeneous turbulence, while in a stratified flow the energy injection rate, flux, and dissipation rate can be strongly affected by the waves. We estimate then $\varepsilon \approx \varepsilon_V$, following the definition in Eq. (4) which corresponds to the effective rate of

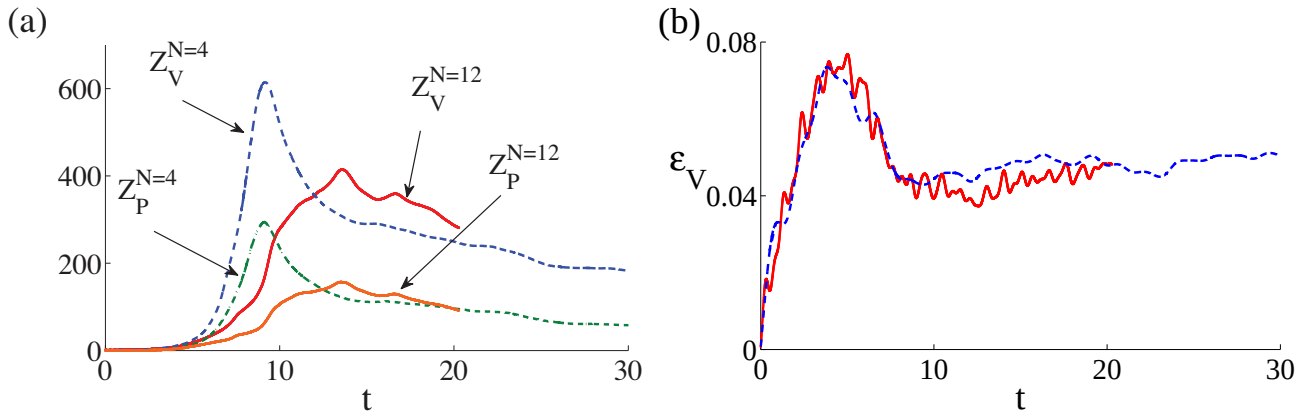

FIG. 2. *(Color online)* Temporal evolution of (a) the kinetic enstrophy $Z_V = \langle|\omega|^2\rangle$ and the potential enstrophy $Z_P = \langle|\nabla\theta^2|\rangle$, and (b) the energy injection rate $\varepsilon_V = \langle \mathbf{u}\cdot\mathbf{f}_V\rangle$ for the runs with $Fr \approx 0.1$ ($N = 4$, dashed lines) and $Fr \approx 0.03$ ($N = 12$, solid lines). More small scales are produced in the less stratified case at earlier times, but both flows evolve towards similar values by the end of the computations.

transfer in the flow. Using ε_V yields a value one order of magnitude smaller for the injection and dissipation rates (see Sec. III A). The estimates obtained in this way are marked by a star in Table I: k^*_{oz} and k^*_η. As will be shown later, these quantities give a better estimation of the scales at which transitions occur in the flow. In practice, a well-resolved run requires $k^*_\eta < k_{\max}$ as dissipation starts to dominate the dynamics at this wavenumber; observe that this is satisfied by our simulations. Also, it can be easily shown that the Ozmidov scale is resolved (e.g., $k^*_{\rm oz} < k^*_\eta$), when $\mathcal{R}_B = ReFr^2 \geq 1$.

A second effective estimate of the vertical characteristic scale, which can be associated with the buoyancy scale, is given by the integral scale based on the parallel potential energy spectrum, as layers tend to develop more clearly in the temperature:

$$L^*_B = 2\pi \frac{\int E_P(k_\parallel)/k_\parallel dk_{||}}{\int E_P(k_\parallel) dk_{||}}. \qquad (13)$$

The corresponding wavenumber $k^*_B = 2\pi/L^*_B = 2$ is also reported in Table I.

Finally, we attempt to assign physical values, characteristic of the atmosphere and the oceans, to the run at the smallest Froude number, with $Fr = 0.03$ and $Re \approx 2.5\times10^4$. For the atmosphere we assume $u_{\rm rms} = 1$ m s^{-1} and $L_0 = 1000$ m (roughly the size of a small convective cell). Hence it is readily found that $N \approx 3.3\times10^{-2}$ s^{-1}, $\nu = 0.04$ m^{2}s^{-1}, and from the simulation presented below, $\varepsilon_V \approx 4\times10^{-5}$m^{2}s^{-3} (per unit mass). Clearly ν is too large for the atmosphere, as expected given the limited grid resolution. However, the energy injection rate is close to atmospheric values, which yield $\varepsilon_V \approx 10^{-6}$–$10^{-5}$m^{2}s^{-3} from data analysis of aircraft measurements [40] and of satellite images [41]. From these values and from the simulation it also follows that $L_B \approx 190$ m and $\ell_{\rm oz} \approx 33$ m, to be compared to the Kolmogorov dissipation scale of ≈ 3 m and to the grid resolution of $\ell_{\min} \approx 1.4$ m.

Runs	$N = 4$	$N = 12$
k_0	1	1
k_F	2-3	2-3
$k_{\max}$	683	683
k_B	4	12
k^*_B	7	8
$k_{\rm oz}$	13	66
$k^*_{\rm oz}$	36	186
k_η	795	795
k^*_η	472	472

TABLE I. Wavenumbers corresponding to the box size (k_0), injection scale (k_F), grid resolution ($k_{\max}$), buoyancy scale (k_B and k^*_B, where wavenumbers without a star are computed using $\varepsilon \approx u^3_{\rm rms}/L_F$, and wavenumbers with stars are computed using the measured injection rate ε_V), Ozmidov scale ($k_{\rm oz}$ and $k^*_{\rm oz}$), and dissipation scale (k_η and k^*_η).

If we consider the ocean instead, the typical velocity is ten times smaller. Hence, given the same Reynolds and Froude numbers, L_B and $\ell_{\rm oz}$ remain the same, while the Brunt-Väisälä frequency and the viscosity are reduced by an order of magnitude. Yet, $\nu = 0.004$ m^{2}s^{-1} is three orders of magnitude larger than realistic values.

III. RESULTS

We first present, in Sec. III A, the temporal behavior of small and large scale quantities integrated over the entire domain. Quantities associated with the dynamics of small scales (Z_V, Z_P and ε_V) reach a steady turbulent regime at an early stage. In contrast, quantities associated with the energetics of the large scales (E_T, $E_{T,fast}$ and $E_{T,slow}$) slowly evolve during the entire calculation. In this case, stationarity is primarily prevented by the monotonic growth of slow modes, as also found for ex-

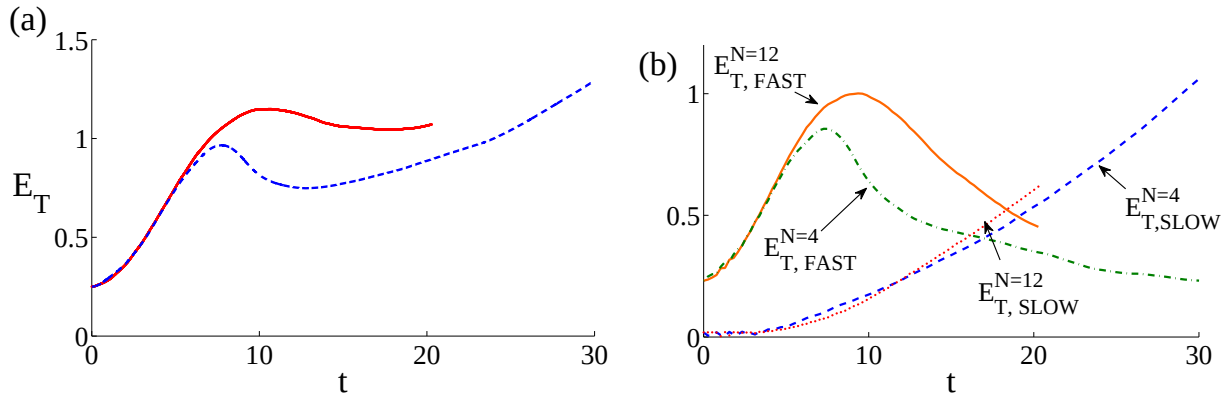

FIG. 3. *(Color online)* (a) Temporal evolution of the total energy for the runs with $Fr \approx 0.1$ ($N = 4$, dashed, blue line) and with $Fr \approx 0.03$ ($N = 12$, solid, red line). (b) Temporal evolution of the energy in the fast and slow modes for the same two runs (see label on the curves). Note the dominance of slow modes as time evolves.

ample in [18]. In Sec. III B we present the energy and helicity distribution among Fourier modes, including a study of spectral anisotropy. Energy and helicity spectra are averaged in time to obtain a representative statistical behavior. Early times are excluded from the average as the turbulent regime is established only after an initial transient in which the flow adapts to the forcing and develops small-scale structures. Finally, in Sec. III C we comment on the energy fluxes.

A. Temporal evolution of global quantities

Fig. 1 shows the ratio between the potential and the total energy as a function of time. The eddy turn-over time is $\tau_{NL} \approx 2.5$. After an initial transient, both curves, independently of the stratification strength, reach a value of $E_P/E_T \approx 0.1$ around $t \approx 14$, followed by a slow monotonic decrease. This ratio is comparable with that found in [10, 12] for similar values of $\mathcal{R}_B$.

In Fig. 2(a) the temporal evolution of the kinetic and potential enstrophy is shown. The initial transient is characterized by the development of small-scales through non-linear mode coupling. This mechanism is less efficient for the more strongly stratified flow as testified by the smaller values of the two enstrophies at early times. This also implies a smaller value of the total energy dissipation $\langle \nu|\omega|^2 + \kappa|\nabla\theta|^2 \rangle$ for the $N = 12$ run. The enstrophy maxima occur earlier in terms of the eddy turnover time (but not in terms of the buoyancy period) for the less stratified flow. Turbulence can be said fully developed beyond the peak of enstrophy where dissipation reaches the smallest scales. Interestingly, at later times, the curves of the two runs merge and undergo a slow decay. This behavior can be identified with the achievement of a turbulent steady state, at least at small scales. Note that as in the case of the ratio E_P/E_T, the enstrophies (and as a result, the energy dissipation rates) also tend to converge to similar values independently of the Froude number.

As a comparison, in Fig. 2(b) we show the temporal behavior of the energy injection rate computed using Eq. (4). The similarity of the two runs is remarkable. A dimensional Kolmogorov-like evaluation of the energy injection rate for fully developed turbulence $\varepsilon \approx u_{rms}^3/L_F$, yields, for our r.m.s. velocity and forcing scale, $\varepsilon \approx 0.4$, an estimate one order of magnitude larger than the numerical value $\varepsilon_V \approx 0.04$. This latter measurement is also compatible with the dissipation rate at late times obtained from $\langle \nu|\omega|^2 + \kappa|\nabla\theta|^2 \rangle$. The order of magnitude difference between the Kolmogorov-like estimation and the actual values of injection and dissipation can be understood as in wave turbulence the energy transfer rate is expected to be smaller than $\approx u_{rms}^3/L_F$ by a factor Fr, as indicated by numerous studies [42, 43]. However, it should be noted that this argument fails to explain why ε_V in the two simulations has similar values independently of the value of Fr. One possibility is that much of the dissipation occurs in the strong gradients that develop in the vertical to ensure that the Froude number based on a characteristic vertical scale is of order unity. If that is the case, the weak turbulence argument can at best apply only to the horizontal dynamics. In other words, a lesser dissipation in the horizontal for smaller Froude number would be compensated almost exactly by an increased dissipation in the vertical. This phenomenon has a counterpart in the anisotropic distribution of energy in spectral space as discussed in the next subsection.

From Fig. 2 we conclude that small scales have saturated, and we remark that the two runs have a tendency towards identical dissipation, a surprising result since the buoyancy Reynolds numbers differ by almost an order of magnitude (but are in both cases above a critical $\mathcal{R}_B \approx 10$). This result is consistent with the recent finding in [9] that the energy spectra are independent of stratification at sufficiently high Reynolds number. However, note that while this is indeed the case for

the spectrum of small scale fluctuations, it is not the case at large scales.

As a first indication of differences at large scales, the time evolution of the total energy is shown in Fig. 3(a). As turbulence develops, the total energy grows until it reaches a peak. At a later stage a fluctuating behavior, characteristic of the turbulent steady state, is expected. However, after the peak, we observe a new monotonic increase with a timescale which is larger than characteristic times such as $1/N$ or τ_{NL}. It is evident from Fig. 3(b) that the energy increase is due to the growth of the slow modes, while the energy in fast modes gradually decreases. We verified on a lower-resolution run and with forcing at substantially smaller scale that the growth of the fast modes saturates after thirty turn-over times, and a steady state of the large scales can also be reached [3].

Several remarks follow from considering the dispersion relation of internal gravity waves

$$\omega = \pm k^{-1}\sqrt{N^2 k_\perp^2}\ .$$

A review of various theoretical approaches to stratified turbulence viewed as a superposition of internal gravity waves can be found for example in [5, 7, 44, 45]. Here it is of interest to recall that three-wave interactions at resonance play a central role in closing the cumulant expansion; in the present case, for a usual triad of modes $\mathbf{k}$, $\mathbf{p}$ and $\mathbf{q}$ satisfying $\mathbf{k} = \mathbf{p} + \mathbf{q}$, they read

$$s_k \frac{k_\perp}{k} = s_p \frac{p_\perp}{p} + s_q \frac{q_\perp}{q},$$

where s_k, s_q and $s_q = \pm 1$ depending on the branch of the dispersion relation used. As remarked in [46, 47], this resonance condition is readily satisfied for $k_\perp \approx p_\perp \approx q_\perp \approx 0$. Hence, it can be inferred that wave-wave interactions lead to a build-up of energy near $k_\perp \approx 0$, i.e., a preferential transfer of energy towards the so-called slow modes. The distinction between energy in fast modes and in slow modes in Fig. 2 is compatible with this build-up of energy in modes with $k_\perp \approx 0$.

The accumulation of energy for $k_\perp = 0$ was already noticed in [29] using a two-point closure of turbulence, the so-called EDQNM2 (Eddy Damped Quasi-Normal Markovian 2 closure). It was also found in [10, 18] using DNS, and related to the growth of the so-called vertically sheared horizontal winds. It is to be noted that such winds, which are off-diagonal elements of the velocity gradient matrix, constitute the vorticity field for negligible vertical velocity and as such they make the velocity field non-potential. In the presence of rotation, these are the so-called thermal winds which are a-geostrophic corrections to geostrophic balance. It is interesting (and may be viewed as somewhat paradoxical) that resonant interactions of gravity waves can lead to the growth of vortical modes which eventually come to dominate the flow.

We finally comment on the temporal dynamics of helicity and relative helicity, $\sigma_V = H_V(E_V Z_V)^{-1/2}$. Although we do not use a helical forcing, we are not imposing the forcing to be completely non-helical. As a result, there is a small amount of helicity in the flow at late times. The time evolution is at follows: helicity starts from zero and it undergoes an oscillatory transient, longer for stronger stratification. In both runs, σ_V then grows slowly in time until it reaches a final value of ≈ 0.12 for the $N = 4$ run. Similarly, and as will be shown later, the relative spectral density $H_V(k)/[kE(k)]$ remains low, of the order of 0.05, except in the vicinity of the forcing scales. These values are too small to affect the energetics of the flows for either runs. In [31] the dynamics of helicity in freely decaying stratified turbulence was examined in terms of a possible balance between its production and dissipation. It was found that only when the initial condition was maximally helical, the energy spectrum was modified by the slowed-down dynamics inherent to the helical case, a situation also found in rotating flows [33]. However, and as shown below, even with a small amount of helicity in the flow, its spectral distribution shows interesting features.

B. Energy distribution across scales

1. *Two-dimensional axisymmetric spectra*

We first show, in Fig. 4, the isocontours of the axisymmetric kinetic energy spectrum, $e_V(k_\perp, k_\parallel)$, normalized by $\sin\Theta$ to yield circular profiles for isotropic flows. When stratification strengthens (Fr decreases) anisotropy increases, i.e., the contours become more visibly stretched along the vertical axis indicating that the energy is mostly concentrated in the slow modes ($k_\perp = 0$). The degree of anisotropy varies across wavenumbers: small wavenumbers (large scales) are more anisotropic than large wavenumbers (small scales). This difference is striking for the less stratified flow [see Fig. 4(a)]. A rough estimate of the recovery of isotropy can be made by considering the wavenumber for which the isocontours approach a circular shape. This occurs at large wavenumbers for $N = 4$, whereas for $N = 12$ isotropy is only barely recovered at the smallest resolved scales.

The axisymmetric total energy spectrum $e(k_\perp, k_\parallel) = e_V(k_\perp, k_\parallel) + e_P(k_\perp, k_\parallel)$ for different values of the co-latitude Θ is plotted in Fig. 5. The dominance of the slow modes (black solid line) is pronounced for both runs; however, these two spectra differ at large scales. While in the $N = 4$ run the spectrum is steep, in the $N = 12$ run the spectrum is shallower and almost flat (see, e.g., [12] for previous observations of a flat spectrum). This has interesting implications: if the energy distribution depends on the stratification strength, the isotropic spectrum, obtained by summing over Θ [see Eq. (8)], will generally vary with Fr. This points to a much richer behavior than for homogeneous and isotropic turbulence as already emphasized in [29].

Moreover, some of the spectra in Fig. 5 are remark-

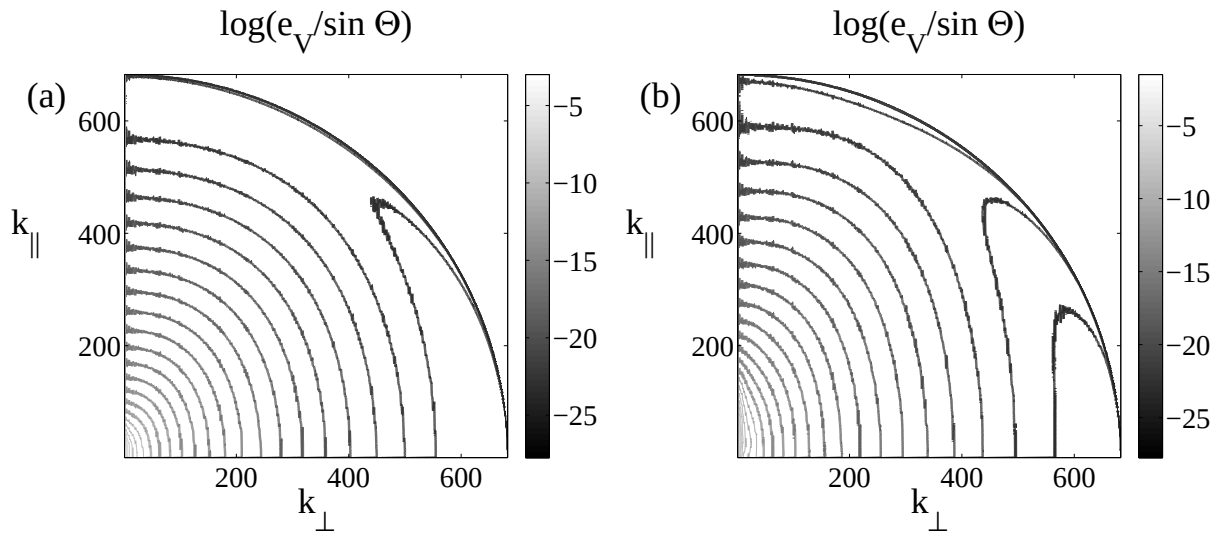

FIG. 4. Contours of the two-dimensional axisymmetric kinetic energy spectrum averaged over time and plotted on a base-10 log scale for the runs with (a) $Fr \approx 0.1$ ($N = 4$) and (b) $Fr \approx 0.03$ ($N = 12$). Note how energy tends to accumulate in slow modes (modes with $k_\perp \approx 0$, also associated with vertically sheared horizontal winds) with elongated isocontours specially at large scales. Isocountours in (b) are more vertically elongated, indicating stronger anisotropy.

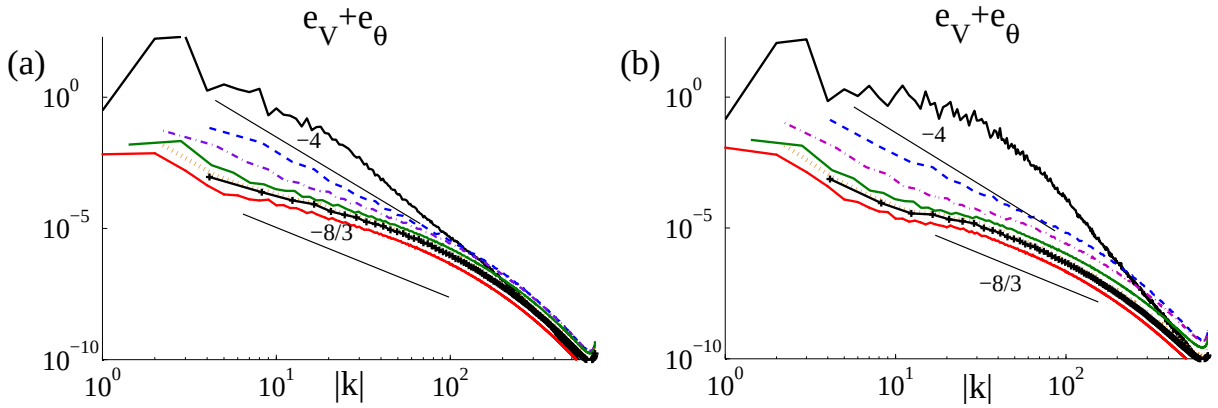

FIG. 5. *(Color online)* Two-dimensional axisymmetric total energy spectra plotted on a base-10 log scale for (a) $Fr \approx 0.1$ ($N = 4$) and (b) $Fr \approx 0.03$ ($N = 12$) for different co-latitudes (with respect to the vertical axis $k_\parallel$ in Fourier space): $\Theta = 0$ (black, solid line), $\Theta \approx 14^\circ$ (blue, dashed line), $\Theta \approx 26^\circ$ (purple, dash-dotted line), $\Theta = 45^\circ$ (green, dash-triple-dotted line), $\Theta \approx 64^\circ$ (yellow, dotted line), $\Theta \approx 76^\circ$ (black, crossed line), and finally $\Theta = 90^\circ$ (red, solid line). Observe the dominance of energy in the $k_\perp = 0$ slow modes ($\Theta = 0$), all the way to the Ozmidov scale where isotropy starts to recover. Solid lines indicate power laws as a reference.

ably steep [note that a spectrum $\sim k^{-4}$ in $e(k_\perp, k_\parallel)$ corresponds, after integration, to a power law $\sim k^{-3}$ in the isotropic spectrum]. For flows whose isotropic spectrum has an inertial index α which falls outside the range $-1 < \alpha < -3$, arguments for locality of interactions do not hold, and interactions between modes can become non-local. Both non-locality, and the existence of different physical regimes, can give rise to non-universality of the spectrum. This has been discussed often in the context of numerous and detailed observations of oceanic and atmospheric flows [45], and also noted for example in the framework of internal waves in the ocean in the hydrostatic (and irrotational) limit [48].

The dominant modes of the weakly stratified run [Fig. 5(a)] scale consistently with a $k_\parallel^{-4}$ power law, the so-called saturated spectrum, whereas a short range of wavenumbers at small scales is compatible with a $k_\perp^{-8/3}$ scaling (corresponding after integration to a Kolmogorov spectrum). Remember that $k_{oz}^* \approx 36$, and note that all angular spectra collapse at smaller wavenumbers indicating that isotropy is recovered. On the other hand, in the strongly stratified run [Fig. 5(b)], $k_{oz}^* \approx 186$ and the spectra only collapse in the dissipative range. It is also interesting and significant to note that the Ozmidov wavenumbers computed with the dynamical injection

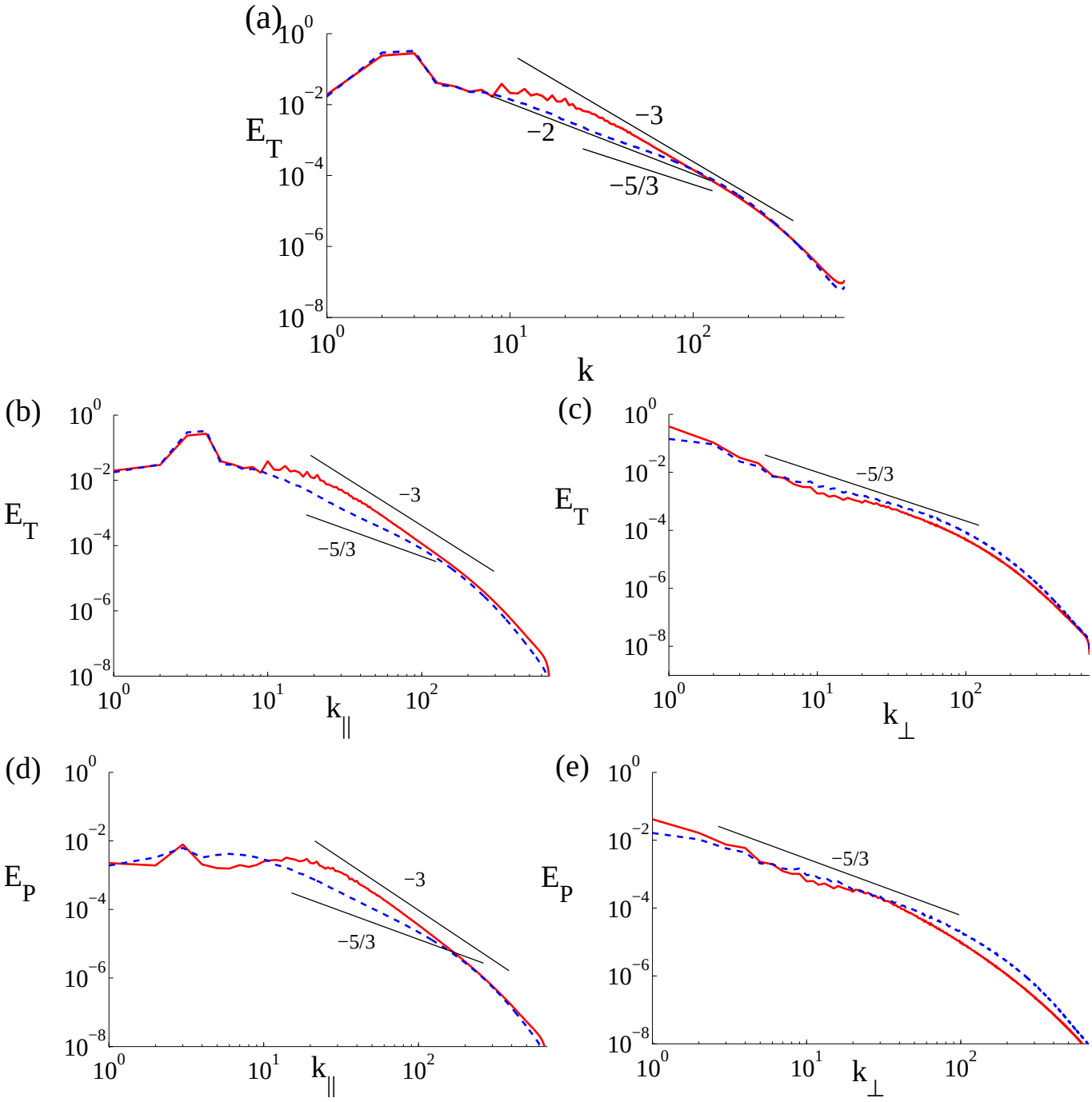

FIG. 6. *(Color online)* Total energy spectra plotted on a base-10 log scale as a function of (a) isotropic wave number, (b) parallel wave number, and (c) perpendicular wave number. The potential energy spectra are shown also as a function of (d) parallel wave numbers, and (e) perpendicular wave numbers. Solid (red) lines correspond to the run with $Fr \approx 0.03$ ($N = 12$ run), while dashed (blue) lines correspond to the run with $Fr \approx 0.1$ ($N = 4$). Solid straight lines indicate some power laws as a reference. The buoyancy scale is identifiable as a break in the potential energy spectrum as a function of $k_\parallel$.

rate, ε_V, ($k^*_{\rm oz}$) mark the transition to isotropy much more reliably than the estimates obtained from Kolmogorov theory $\varepsilon \sim u^3_{\rm rms}/L_F$ ($k_{\rm oz}$).

Due to the fact that different inertial ranges can be present in stratified flows, the resolution employed in our computations (although high) is insufficient to clearly state whether the regimes that are expected on a phenomenological basis are actually present. We therefore warn the reader that scaling laws are only indicated as a reference, and to point out the compatibility of the

results with theoretical or phenomenological arguments: namely, the idea that the perpendicular modes and all the modes larger than k_{oz} follow a Kolmogorov scaling, whereas parallel modes in the range where waves dominates follow a saturated spectrum.

Finally, in Ref. [17] it is suggested to analyze the data once the slow modes ($k_\perp = 0$) are removed. The analysis of the flow in terms of two-dimensional spectra allows for such a reduction, since the $k_\perp = 0$ modes are confined to the $\Theta = 0$ angle (black solid line in Fig. 5). The $\Theta = 0$ spectrum is clearly distinguishable from the other curves when stratification is large. Remarkably however, the spectral slopes of the remaining curves seem to separate into two sets, one that follows the behavior of the small Θ spectra, and another that mimics the $\Theta = \pi/2$ spectrum.

2. *The resulting one-dimensional energy spectra*

We now consider the one-dimensional (i) isotropic, (ii) parallel, and (iii) perpendicular spectra for the total energy and the potential energy, see Fig. 6. The spectra are averaged in time from the peak of enstrophy to the final time. It was remarked in [29] that two-dimensional spectra (Figs. 4 and 5) may represent a more realistic diagnostics of anisotropic flows given the wide variety of slopes displaied as a function of the angle Θ and the imposed stratification. While this is clear from the previous analysis, the Ozmidov scale and the buoyancy scale will show up more clearly in some of the reduced spectra.

Figure 6(a) shows the isotropic total energy spectrum for both runs. The spectrum displays a peak associated with the forcing wavenumber, followed by a flat range which extends until about k_B (see Table I). The parallel spectrum of the total energy $E_T(k_\parallel)$ [Fig. 6(b)], and more evidently, the parallel spectrum of the potential energy $E_P(k_\parallel)$ [Fig. 6(d)] are also flat at large scales. On the other hand, the perpendicular spectra in Fig. 6(c) and Fig. 6(d) are consistent with a $\sim k^{-5/3}$ power law at all scales, independently of the stratification as noted in [21]. The scale at which the flat spectrum ends seems to depend linearly on the Froude number.

The flatness of the isotropic spectra at large scales is due to the combination of two related factors: (i) the dominance of the $k_\perp = 0$ modes, and (ii) the organization of the flow in the vertical direction in well-defined strata with strong vertical gradients both in the velocity and in the buoyancy field. It was shown, for example in [12], that a superposition of such strata can lead to a flat spectrum since, at large scales, these layers can be interpreted as quasi-discontinuities.

The buoyancy scale is generally understood in the context of theoretical studies (see, e.g., [27]) by advocating that the development of turbulence in the vertical direction leads to an effective vertical Froude number $Fr_z = u_{\rm rms}/[L_B^* N]$ of order unity. In a different context, the buoyancy wavenumber was introduced before in [24] to take into account the fact that, in the Lagrangian framework, the buoyancy field is advected by the velocity (although not as a passive scalar) and thus should depend on the total kinetic energy. This leads to the prediction of a sharp break in the buoyancy flux spectrum $\langle w\theta \rangle$ at k_B, a break that should not develop in the kinetic energy spectrum.

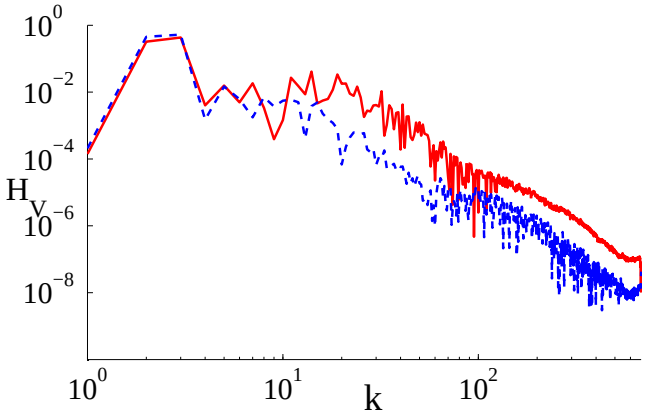

FIG. 7. *(Color online)* Spectrum of the absolute value of helicity plotted on a base-10 log scale. Solid (red) lines correspond to the run with $Fr \approx 0.03$ ($N = 12$ run), while dashed (blue) lines correspond to the run with $Fr \approx 0.1$ ($N = 4$). Note the flat spectra at large scale, up to what can be identified as the buoyancy scale.

As one moves to larger wavenumbers, the layers begin to be resolved and their intrinsic dynamics arises. There, the run with $N = 12$ shows a steep spectrum compatible with $\sim k^{-3}$, the so-called "saturated spectrum" which corresponds to a balance in the vertical between nonlinear advection and buoyancy. For weaker stratification (dashed blue curve) the saturated spectrum does not have enough scales to develop and instead one observes an overall slope close to k^{-2} extended on one decade. The collapse of the anisotropic spectra for different Θ explains the shallower and Kolmogorov-like spectrum for wavenumbers larger than $k_{\rm oz}^*$. Note that using large-eddy simulations, the transition from a steep (saturated) large-scale spectrum to a Kolmogorov isotropic spectrum was observed before in [49] but only sporadically, when breaking events occurred and the turbulence was thus more vigorous.

Finally, Fig. 7 shows the spectrum of the absolute value of helicity for both simulations. Although helicity is rather small and not important for the flow dynamics, the spectra display a flat region at large scales followed by a decay at smaller scales with a break near the buoyancy scale, similarly to the decay runs in Ref. [31]. There are rapid changes of sign in the small scales, manifesting as large fluctuations. Interestingly, flat helicity spectra in the planetary boundary layer have been observed at night when the flow is more stably stratified [50].

C. Energy fluxes

An examination of energy fluxes confirms the analysis presented in the preceding section. The two simulations, at buoyancy Reynolds numbers of ≈ 27 and ≈ 220 respectively, behave differently as to how the energy is being transferred among scales, as can be seen in Fig. 8 which displays the kinetic, potential, and total energy fluxes for both runs. Note that the flux constructed from taking only the dot product of Eq. (1) with the velocity (i.e., the "kinetic energy flux") is not a flux, in the sense that its divergence is not zero (i.e., kinetic energy is not conserved alone). Instead, this "flux" should be interpreted as energy flux plus power: when it is larger than zero, kinetic energy is transferred towards smaller scales by the velocity field, or injected per unit of time by work done by the temperature. The same applies to the "potential energy flux" constructed from dotting Eq. (3) with the temperature fluctuations: when it is positive, potential energy is transferred towards smaller scales or injected by work done by the velocity, while when it is negative potential energy may be removed by work done by the velocity. Only the total energy defines a proper flux, in the sense that its sign is solely associated with direction of transfer across scales, and in the sense that it goes to zero for $k \to \infty$ (i.e., the total energy is conserved).

In the less stratified run with $N = 4$ (high buoyancy Reynolds number $\mathcal{R}_B$), the total energy flux is approximately constant in a range of wavenumbers that in fact defines the inertial range, with amplitude $\approx 2.7 \times 10^{-2}$. The potential and kinetic energy flux, in the light of the total flux, then indicate how energy is exchanged between the velocity field and the temperature. The potential energy flux is zero at large scale and rather small ($\approx 5 \times 10^{-4}$, or roughly 2% of the kinetic energy flux) in the same inertial range. It becomes negative and progressively larger (in absolute value) at small scale (after $k \approx 40$), at the end of the inertial range and for $k = k_{\max}$, it reaches $\approx -7 \times 10^{-3}$, a value compensating the kinetic flux at that wavenumber, a condition necessary for energy conservation. The negative value of this flux at small scales indicates that energy is transferred from the small scale temperature fluctuations to the velocity field fluctuations (or in other words, that the small scale temperature gradients exert work on the velocity field, exciting small scale motions). This is in good agreement with the evolution of the enstrophies observed in Fig. 2: more energy is dissipated by small scale velocity fluctuations (i.e., by the kinetic enstrophy) than by temperature fluctuations (whose dissipation is associated with the potential enstrophy). Energy at small scales then is transferred from the temperature to the velocity, where it is finally dissipated.

The dynamics of energetic exchanges is rather different at low $\mathcal{R}_B$. Although the same trends are observed, there is barely a range where the total energy flux is constant; furthermore, all three fluxes are larger in amplitude, but the ratio of kinetic to potential flux is now only roughly equal to 5 at large scales and the potential flux becomes negative at a higher wavenumber (≈ 100). One is led to the conclusion that, at that Froude number (and buoyancy Reynolds number), the flow is not sufficiently turbulent even though it produces strong gradients in the vertical.

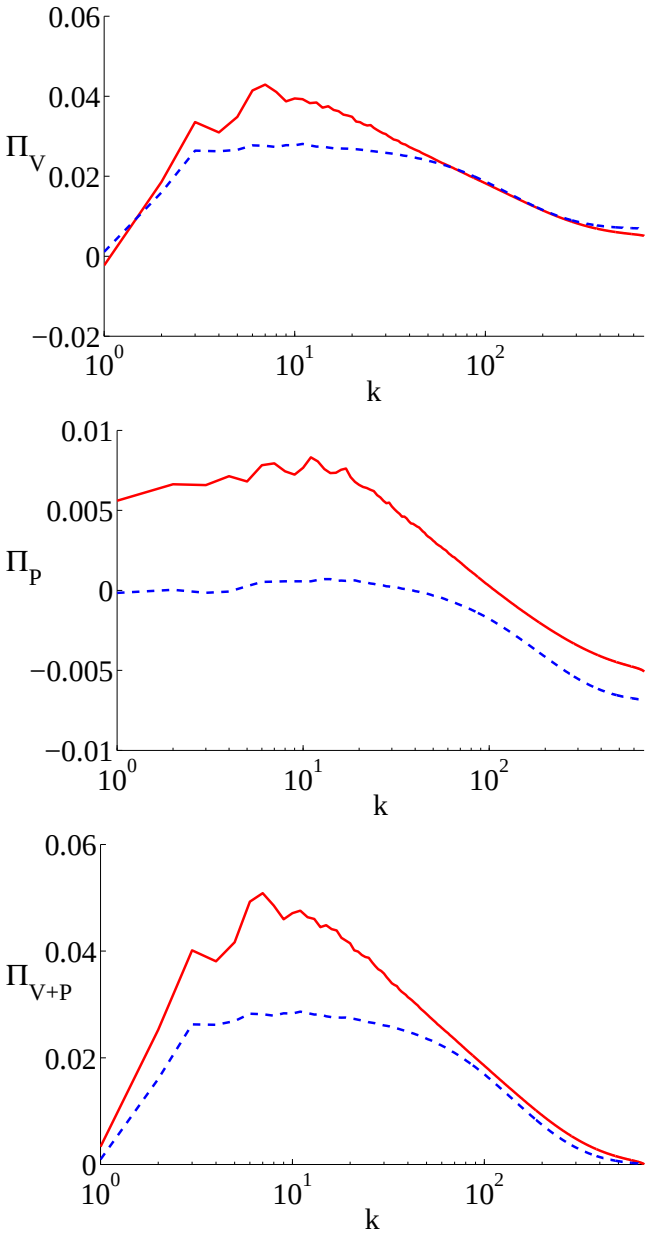

FIG. 8. *(Color online)* Fluxes of kinetic (top), potential (middle) and total (bottom) energy plotted on a base-10 log scale for the runs with $Fr \approx 0.1$ ($N = 4$, indicated by the dashed blue line), and with $Fr \approx 0.03$ ($N = 12$, solid red line).

IV. DISCUSSION AND CONCLUSION

We performed high resolution direct numerical simulations of stably stratified turbulence for Reynolds number equal to $Re \approx 25000$ and Froude numbers $Fr \approx 0.1$ and $Fr \approx 0.03$. The stratified flow is modeled using the Boussinesq equations, integrated numerically in a triply-periodic cubical domain of dimensionless volume $V = (2\pi)^3$, discretized with an isotropic grid of 2048^3 points. The flow is forced at large scale ($k_F = 2$ and 3) by a three-dimensional randomly generated velocity field. By contrasting the behavior of the two simulations we identify some similarities despite the fact that the buoyancy Reynolds number differs by almost an order of magnitude: after an initial transient the two runs have comparable values of the kinetic and potential enstrophy (Z_V, Z_P) and of the energy injection rates (ε_V). The same ratio between potential and total energy ($E_P/E_T \approx 0.1$) is also spontaneously selected by the flows. For both values of Fr, slow modes grow monotonically as a consequence of nonlinear interactions and cause a moderate increase of the total energy (E_T) in time.

The axisymmetric kinetic energy spectrum $e_V(k_\perp, k_\parallel)$ clearly reveals the anisotropy of the flow, which manifests up to the highest wavenumbers for the $Fr \approx 0.03$ run. The axisymmetric total energy spectrum $e_V + e_\theta$ shows a wide variety of spectral slopes as a function of the angle Θ between the imposed stratification and the wavevector. The slow modes, corresponding to $\Theta = 0$ (i.e., to $k_\perp = 0$), are visibly dominant and their spectrum is flat at large scale for the strongly stratified run. Moreover, the $\Theta = 0$ spectrum is clearly distinguishable from the other curves, specially when stratification is large. Remarkably however, the spectral slopes for the remaining curves with $\Theta \neq 0$ seem to separate into two sets, one that follows the behavior of the small Θ spectra, another that mimics the $\Theta = \pi/2$ spectrum. All these spectra collapse at a scale which is consistent with the Ozmidov length scale calculated with the dynamical injection rate.

As the isotropic total energy spectrum is the result of the superposition of these different dynamical regimes, its interpretation is difficult. It is roughly flat from the forcing scale k_F up to the buoyancy scale k_B. At intermediate scales, a k^{-3} power law appears for the $Fr \approx 0.03$ run, which is the signature of the saturation spectrum that characterizes the energetically dominant slow modes. This saturation spectrum is also consistent with the simple 1D model presented in [2]. When $Fr \approx 0.1$ the saturation spectrum does not have enough scales to develop and one observes a shallower slope in the isotropic spectrum well approximated by a k^{-2} power law and compatible with a Kolmogorov scaling $k^{-5/3}$ in the small scale end of the inertial range.

Finally, the spectrum of helicity (velocity-vorticity correlations) is rather weak in relative terms, and behaves as previously observed in freely decaying simulations [31]: it is flat from k_0 to k_B. This was also reported for the nocturnal planetary boundary layer, and is in remarkable agreement with recent observations that show that, for more stably stratified flows, the spectrum of helicity evolves toward a flat distribution [50].

As it appears from our results and as also noted in the literature, the dynamics of stratified turbulence proves to be more complex than the homogeneous isotropic case, specially at intermediate values of the buoyancy Reynolds number, when waves and eddies strongly interact. Further studies are needed, in particular because there are several relevant scales that must be separately resolved, and which can be differently ordered according to the values of the external parameters. For example, depending on Fr and Re the Ozmidov scale could be either smaller or larger than the dissipative scale, or the buoyancy and Ozmidov scales could be well separated or comparable. Also, the forcing could be at smaller scales that what is chosen in this paper. Since large resolution is needed to study problems with multiple length scales, and as computer resources are insufficient to study realistic scale separations, we have to study individual cases and rely on comparisons with previous studies to identify possible regimes, and to identify features that are robust to changes in the parameters. The parameters chosen here are intended to represent a likely physical scenario for geophysical flows, even though Reynolds numbers are clearly much lower than in realistic cases.

To conclude, we briefly mention an open question in the field. A relevant issue concerns the effect that the forcing has on the outcome of the simulations, which is far from evident (see for example the discussion in [49]). In our studies, isotropic forcing (and initial conditions) were used to prevent a possible bias in the development of anisotropies (i.e., of angular variations in spectral space). However, differences may arise when other forcings, or when correlations between the temperature and the velocity field, are imposed. We leave this problem for future studies.

C.R. acknowledges support from two RSVP/CISL grants. Computer time on Yellowstone through an ASD allocation was provided by NCAR under sponsorship of NSF.

[1] D. H. Lenschow, M. Lothon, S. D. Mayor, P. P. Sullivan, and G. Canut, Bound. Lay. Met. **143**, 107 (2012).
[2] C. Rorai, P. D. Mininni, and A. Pouquet, Phys. Rev. E **89**, 043002 (2014).
[3] R. Marino, P. D. Mininni, D. L. Rosenberg, and A. Pouquet, Phys. Rev. E **90**, 023018 (2014).
[4] J. Riley and M.-P. Lelong, Ann. Rev. Fluid Mech. **32**, 249 (2000).
[5] C. Staquet and J. Sommeria, Ann. Rev. Fluid Mech. **34**, 559 (2002).

[6] J. McWilliams, in Atmospheric turbulence, edited by E. Fedorovich, R. Rotunno, and B. Stevens (Cambridge University Press, 2004) pp. 35–49.
[7] P. Sagaut and C. Cambon, Homogeneous Turbulence Dynamics (Cambridge University Press, Cambridge, 2008).
[8] M. L. Waite, Laboratory-scale stratified turbulence, Vol. to appear, Modeling Atmospheric and Oceanic Flows: Insights from Laboratory Experiments and Numerical Simulations, American Geophysical Union Monograph (T. von Larcher and P. Williams (eds.), 2014).
[9] P. Bartello and S. Tobias, J. Fluid Mech. **725**, 1 (2013).
[10] G. Brethouwer, P. Billant, E. Lindborg, and J.-M. Chomaz, J. Fluid Mech. **585**, 343 (2007).
[11] M. L. Waite, Phys. of Fluids **23**, 066602 (2011).
[12] Y. Kimura and J. R. Herring, J. Fluid Mech. **698**, 19 (2012).
[13] S. Almalkie and S. de Bruyn Kops, J. Turbulence **13**, 29 (2012).
[14] S. de Bruyn Kops, APS/DFD abstract, see http://meetings.aps.org/link/BAPS.2013.DFD.A23.4 (2013).
[15] S. de Bruyn Kops, Preprint (2014).
[16] D. C. Fritts, L. Wang, and J. Werne, Geophys. Res. Lett. **66**, 1149 (2009).
[17] D. Chung and G. Matheou, J. Fluid Mech. **696**, 434 (2012).
[18] L. Smith and F. Waleffe, J. Fluid Mech. **451**, 145 (2002).
[19] R. Marino, A. Pouquet, and D. Rosenberg, Phys. Rev. Lett. **114**, 114504 (2015).
[20] D. Rosenberg, A. Pouquet, R. Marino, and P. D. Mininni, Phys. Fluids **27**, 055105 (2015).
[21] E. Lindborg and G. Brethouwer, J. Fluid Mech. **586**, 83 (2007).
[22] L. Shih, J. Koseff, G. Ivey, and J. Ferziger, J. Fluid Mech. **525**, 193 (2005).
[23] G. Ivey, K. Winters, and J. Koseff, Ann. Rev. Fluid Mech. **40**, 169 (2008).
[24] J. Weinstock, J. Atmos. Sci. **35**, 634 (1978).
[25] A. Craya, Publ. Sci. Tech. Ministère de l'Air **345** (1958).
[26] J. R. Herring, Phys. Fluids **17**, 859 (1974).
[27] P. Billant and J.-M. Chomaz, Phys. Fluids **13**, 1645 (2001).
[28] O. Métais and J. Herring, J. Fluid Mech. **202**, 117 (1989).
[29] F. Godeferd and C. Cambon, Phys. Fluids **6**, 2084 (1994).
[30] T. J. McDougall, R. J. Greatbatch, and Y. Lu, Journal of Physical Oceanography **32**, 1574 (2002).
[31] C. Rorai, D. Rosenberg, A. Pouquet, and P. D. Mininni, Phys. Rev. E **87**, 063007 (2013).
[32] P. D. Mininni and A. Pouquet, Phys. Rev. E **79**, 026304 (2009).
[33] T. Teitelbaum and P. D. Mininni, Phys. Rev. Lett. **103**, 014501 (2009).
[34] R. Hide, Geophys. Astrophys. Fluid Dyn. **7**, 157 (1976).
[35] R. Marino, P. D. Mininni, D. Rosenberg, and A. Pouquet, Phys. Rev. E **87**, 033016 (2013).
[36] P. D. Mininni, D. Rosenberg, and A. Pouquet, J. Fluid Mech. **699**, 263 (2012).
[37] P. D. Mininni, D. Rosenberg, R. Reddy, and A. Pouquet, Parallel Computing **37**, 316 (2011).
[38] A. Pouquet and G. S. Patterson, J. Fluid Mech. **85**, 305 (1978).
[39] P. D. Mininni, A. Alexakis, and A. Pouquet, Phys. Rev. E **77**, 036306 (2008).
[40] E. Lindborg, J. Fluid Mech. **388**, 259 (1999).
[41] P. Héas, E. Mémin, D. Heitz, and P. D. Mininni, Tellus A **64**, 10962 (2012).
[42] A. Newell, S. Nazarenko, and L. Biven, Physica D **152-153**, 520 (2001).
[43] S. Nazarenko, Wave Turbulence, Vol. **825** (Springer-Verlag, 2011).
[44] P. Müller, G. Holloway, F. Henyey, and N. Pomphrey, Rev. Geophys. **24**, 493 (1986).
[45] K. Polzin and Y. Lvov, Rev. Geophys. **49**, RG4003 (2011).
[46] F. Waleffe, Phys. Fluids **A5**, 677 (1993).
[47] L. M. Smith and F. Waleffe, Phys. Fluids **11**, 1608 (1999).
[48] Y. Lvov, K. Polzin, E. Tabak, and N. Yokoyama, J. Phys. Oceano. **40**, 2605 (2010).
[49] G. Carnevale, M. Briscolini, and P. Orlandi, J. Fluid Mech. **427**, 205 (2001).
[50] B. Koprov, V. Koprov, V. Ponomarev, and O. Chkhetiani, Dokl. Phys. **50**, 419 (2005).